Transactions of the SMiRT 27
Yokohama, Japan, March 3-8, 2024
Division I

Microstructural Evolution due to CO_2 Oxidation and Carburisation in Fe9Cr1Mo Steel

Peter Thomas, Mariia Zimina[2], Aya Shin[3], Jonathan Pearson[4], Peter E J Flewitt[5] and Tomas Martin[6]

[1] PhD Researcher, School of Physics, University of Bristol, Bristol, U.K (peter.j.thomas@bristol.ac.uk)
[2] Senior Research Associate, School of Physics, University of Bristol, U.K
[3] R&D Nuclear, Research and Development, EDF U.K
[4] Chemistry & CO_2 Oxidation Group, Nuclear Operation, EDF U.K
[5] Honorary Professor in Materials, School of Physics, University of Bristol, U.K
[6] Associate Professor in Materials Physics, School of Physics, University of Bristol, U.K

ABSTRACT

Understanding the type, size, and distribution of precipitates in the microstructure of metals is important to understand their material properties and evolution, but many characterisation techniques struggle to distinguish precipitates from the surrounding matrix. By using gaseous XeF_2 contrast mapping in conjunction with image processing we can gain statistical insight into precipitates and their evolution within steel. XeF_2 gas is used to induce ion channelling contrasts with a focused ion beam (FIB) on an experimental Fe9Cr1Mo steel sample. Precipitates and substructures are made evident by the gas and statistical information for the precipitates such as: type, size, shape, and distribution were extracted. The technique provides a significant statistical improvement for 2D precipitate characterisation and evaluation compared to more commonly adopted methods and should be a standard technique in every microscopist's toolkit.

INTRODUCTION

Investigations into the type, size, and distribution of precipitates as a materials microstructure evolves are of key importance when understanding the change chemical, physical and mechanical properties that can occur in steels at all length-scales through time. Precipitates such as carbides can form in intergranular and intragranular regions of alloys such as the steels used in structural applications in the electrical power generation, aerospace, and automotive industries. Carbide precipitates can pin and therefore limit the movement of dislocations and indeed weaken surrounding regions by depleting the matrix in certain elements and hinder dynamic recrystallisation. Overall the presence of such precipitates can make the particular steel more susceptible to corrosive attack, and modify crack initiation and propagation and/or fracture mode (see Advani et al. (1991), Callister and Rethwisch (2020), Hwang et al. (2013), Li et al. (2019) and Liu et al. (2023)).

In 2D optical microscopy, there are many different approaches to gaining information on the characteristics of precipitates within a steel . A well-established procedure has been to use selective etchants to identify different phases (see Petzow et al. (1978)), but it is difficult to distinguish between different carbide precipitate types and is limited by the resolution of the optical microscope. Some precipitates can be distinguished using scanning electron microscopy (SEM) combined with energy-dispersive X-ray spectroscopy (EDX) and electron backscatter diffraction (EBSD). However, it is difficult to detect and quantify carbon using EDX elemental signatures and many carbide precipitates have similar diffraction patterns in EBSD, making them hard to distinguish. To obtain high-resolution images of precipitates at the nano-metre length-scale, scanning / transmission electron microscopy (S/TEM) provides morphology, atomic arrangement, and electron diffraction information to give unique precipitate identification. Unfortunately, the selected imaging areas are too small to gather appropriate statistical information.

This is where the FIB-XeF_2 contrast mapping technique is of help when considering 2D areas of interest. By introducing XeF_2 gas, during imaging using a Ga FIB, one can suppress ion channelling, creating an image with a contrast that depends primarily on the work function of the material over larger length-scales (see Liu et al. (2019)). This gives different types of precipitates a variation of greyscale contrast during FIB imaging, allowing them to be identified and analysed with image processing software. This approach can be combined with small-scale diffraction techniques to identify each object type for the entire data set. Some examples of FIB-XeF_2 contrast mapping in the literature can be found in studies by Coghlan (2020), Gong et al. (2023), Liu (2018) and Yan et al. (2018).

FIB-XeF_2 contrast imaging is not a widely adopted procedure. The XeF_2 gas module is a common addon to dualbeam microscopes for the purposes of gas-assisted etching. By using XeF_2 gas with either a focused-electron beam (see Ganczarczyk et al. (2010)) or focused-ion beam the interaction reduces re-deposition of material (see Kettle et al. (2009) and Ray et al. (2016)). This allows the creation of lithographic nanostructures, used in integrated circuits (see Lawson and Robinson (2016)) and other thin film devices (see Aassime and Hamouda (2017). By taking advantage of the common availability of XeF_2 gas modules on dualbeam microscopes, it can easily be repurposed for use in metallurgy.

While the FIB-XeF_2 contrast imaging technique is sometimes used, it has not often been fully exploited. In this paper, we characterise precipitates within a carburised steel sample by using the FIB-XeF_2 contrast 2D mapping technique. In doing so we quantify the type, size and distribution of precipitates present and their statistical properties at a pixel-by-pixel resolution. This work shows a breakdown of area fraction by precipitate type and the distribution alongside a statistical breakdown of quantified properties over relatively large distances (i.e., 2mm). This study expands on the basic procedure of the FIB-XeF_2 contrast mapping and combined with image processing, provides an example of detailed quantification of carburisation in hot CO_2-gas exposed Fe9Cr1Mo steel, which is relevant to the operation of high-temperature gas-cooled nuclear reactors.

EXPERIMENTAL PROCEDURES AND MATERIAL

The sample of interest is an experimental Fe9Cr1Mo steel with the geometry of a finned boiler tube (see Figure 1). Fe9Cr1Mo steels have 9 wt.% Cr, 1 wt.% Mo with the balance made of predominantly Fe and minor elemental additions. The experimental sample was exposed to a simulated reactor gas of primarily CO_2, simulating the reactor gas of the advanced gas-cooled reactors (AGRs) primarily found in the U.K. The environment was maintained at a temperature of 580°C, with total exposure lasting >118k hrs. The sample was exposed to the simulated reactor environment on both the inner and outer surface of the finned tube. During long-term exposure to CO_2 at these temperatures, steels form a complex oxide structure on the

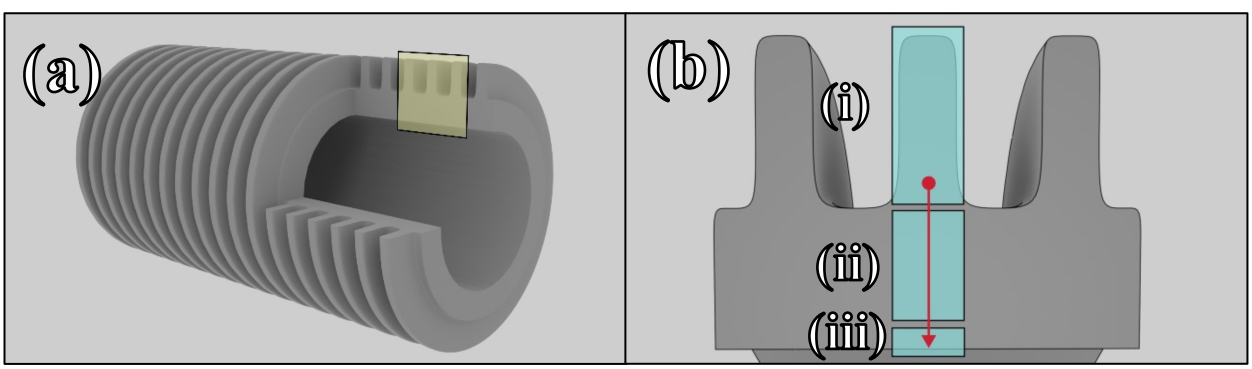

Figure 1: Example geometry of Fe9Cr1Mo steel finned tubes that was used in this study. a) Finned tube with a quadrant removed to display cross sectional geometry. Highlighted region refers to subfigure b). b) Cross section of the finned tube, i) Fin, ii) Bulk, iii) Bore. Red line indicates direction and path the data was collected through.

surface, and carbon ingress into the metal creates substantial numbers of new carbide precipitates of different forms, making this type of specimen an ideal test case for the FIB-XeF_2 contrast mapping technique. More detail on the process of oxidation-carburisation of these materials can be found in in studies by Coghlan (2020), Karunaratne et al. (2020), Liu (2018), Yan et al. (2018) and Young and Zhang (2018). The sample was prepared for study via a longitudinal cross-sectioning, mounted in graphite to expose the cross-section presented in Figure 1.b, and finished with a colloidal silica polish.

FIB-XeF_2 Contrast Mapping

The FIB-XeF_2 contrast mapping technique was applied to bring out a visible contrast between precipitates, their substructures, and the matrix in this steel. With these FIB-XeF_2 micrographs, image processing was then applied in Dragonfly [Computer Software] (2022) to identify many regions of interest (ROIs) using Otsu thresholding (see N. Otsu (1979)) of the different contrast features highlighted by the FIB-XeF_2. The identity of the precipitates in each of these different contrast ROI categories were then identified using transmission Kikuchi diffraction (TKD). Once a ROI had been isolated from the matrix and other ROIs, precipitate quantification was achieved, answering the question: What is the area fraction of a specific type of precipitate? Further object analysis was also done within the software, allowing further questions to be answered, such as: What is the number density of a specific precipitate? What are they shaped like? and how big are the precipitates?

The FIB-XeF_2 contrast mapping procedure and micrograph capture were collected using a ThermoFisher Scios 2 dual-beam system, which contains a gallium ion source. The procedure used in this study was a modification of previous procedures described by Coghlan (2020), Gong et al. (2023), Liu (2018), and Yan et al. (2018), as such the procedure will be described in full. Alterations to these methodologies were done to bring out the contrast slowly at a much lower magnification to enable substructure contrasts that were visible over large areas.

The FIB was set up as follows:

- Probe current: 50 nA,
- Probe potential: 30kV,
- Working distance: 19mm,
- Magnification: 500x,
- Resolution: 1536 x 1024,
- Dwell time 50 ns.

Firstly, an exposure to the area of interest was run for approximately 20 seconds at 50nA, this was done to remove the surface oxide layer and expose hard precipitates in the matrix. After the initial exposure, the beam is blanked and the XeF_2 gas is introduced near the area of interest for 5-10 seconds via a gas injection system (GIS) needle, to alter the work function of the matrix and precipitates. Once the GIS needle was retracted the area of interest was then exposed to a much lower current of 1 nA with the same initial parameters, but now with a dwell time of 1 µs. This was continued until all the precipitates and their substructures were visible (the darkest precipitates appear first), and a high-resolution image was taken. In this study, the final images were taken at a resolution of 6144 x 4096, integrated 4 times with a dwell time of 1 µs. This produced an image of significant quality for quantitative analysis without altering the contrast too much. The stage was then moved down the sample from the fin region into the bore region (see Figure 1.b) in increments of 300 µm. This led to a series of eight images covering a total distance of ~2mm.

Transmission Kikuchi Diffraction (TKD) was performed using a ThermoFisher Helios 5 Hydra dual-beam system on lamella lift-outs for the distinct regions of interest visible in the FIB micrographs. TKD was obtained using an Oxford Instruments Symmetry S2 EBSD detector with a SEM beam of 30 kV and EBSD camera exposure time of 25ms. Diffraction patterns were obtained for each of the different geometries of precipitate observed in the FIB-XeF_2 mapping.

Image Processing and Analytical Techniques

Image processing was performed using Dragonfly [Computer Software] (2022) for Windows. The same image processing was applied to all images pre-analysis. To prepare the images for analysis they were first filtered using median smoothing within Dragonfly [Computer Software] (2022), to remove 'salt and pepper' noise, while keeping detail. Image look-up-tables (LUTs) were then ranged to only include the main peaks and to exclude redundant data. Images were then cropped to remove any edge effects caused by the XeF_2 procedure, including all unintended altered image contrast.

After image preparation the images a round of thresholding was performed using the automatic Otsu threshold selection method (auto-Otsu, see N. Otsu (1979)) within Dragonfly [Computer Software] (2022). Splitting the image into foreground and background based upon greyscale contrast values, where the precipitates were separated from the matrix. The auto-Otsu was then applied again to the precipitate group, separating the precipitates into ROIs of light and dark. One final auto-Otsu was used to separate the dark ROI precipitates into two dark precipitate ROIs where one of the groups was darker than the other.

Post-processing was then applied to the three ROIs, where manual and automated adjustments were made to remove artefacts, false precipitate connectivity and other unwanted areas (such as dirt, pits etc). This included the 'open' morphological operation on the ROIs, whereby an erosion is followed by a dilation, this was done to remove the 'haloing' of light ROIs around dark ROIs caused by a minor gradient between dark precipitate and matrix. Finally, areas within a ROI smaller than 50 voxels were removed to try and exclude any trace dirt, indent or other artefact-creating effects created by sample preparation and transport.

Area and object analysis was performed on the three ROIs within Dragonfly [Computer Software] (2022). Firstly, a slice analysis was performed within the images to produce the ROI area fraction per pixel row. This data was then reduced by taking a sampling interval of 10 data points and taking the mean, the standard deviation was calculated using a moving standard deviation of $\pm$ 5 data points on the raw data and then reduced in the same manner.

Object analysis was completed in Dragonfly [Computer Software] (2022) by separating the ROIs into multi-ROIs, whereby each separated object within a ROI becomes its own ROI within a collection of a multi-ROI. All objects connected to the edge surface of the image were removed to exclude partial objects. Scalar statistics of surface area, aspect ratio and position for each set of multi-ROIs were then extracted and presented as number density by distance where possible and by relative frequency/fraction elsewhere. The aspect ratio was calculated as the ratio of the minimum and maximum inertia eigenvectors. This leads to an aspect ratio of 0 for a perfect rod and a value of 0.5 for a perfect circle.

RESULTS

XeF_2 Contrast Mapping and ROI Characterisation

FIB-XeF_2 contrast mapping procedure revealed several areas of interest that varied in both greyscale and morphology, see Figure 2 and Table 1. The differences in greyscale were sufficient for clear separation of objects indexed as 1 ($M_{23}C_6$), 2 (M_7C_3) and 4 (M_2C). However, objects 3 (substructure within $M_{23}C_6$) and 4 (M_2C) had greyscale values too close to distinguish. $M_{23}C_6$ was found both intergranularly and intragranularly. M_7C_3 were predominantly found intergranularly, while M_2C was found in intragranular clusters.

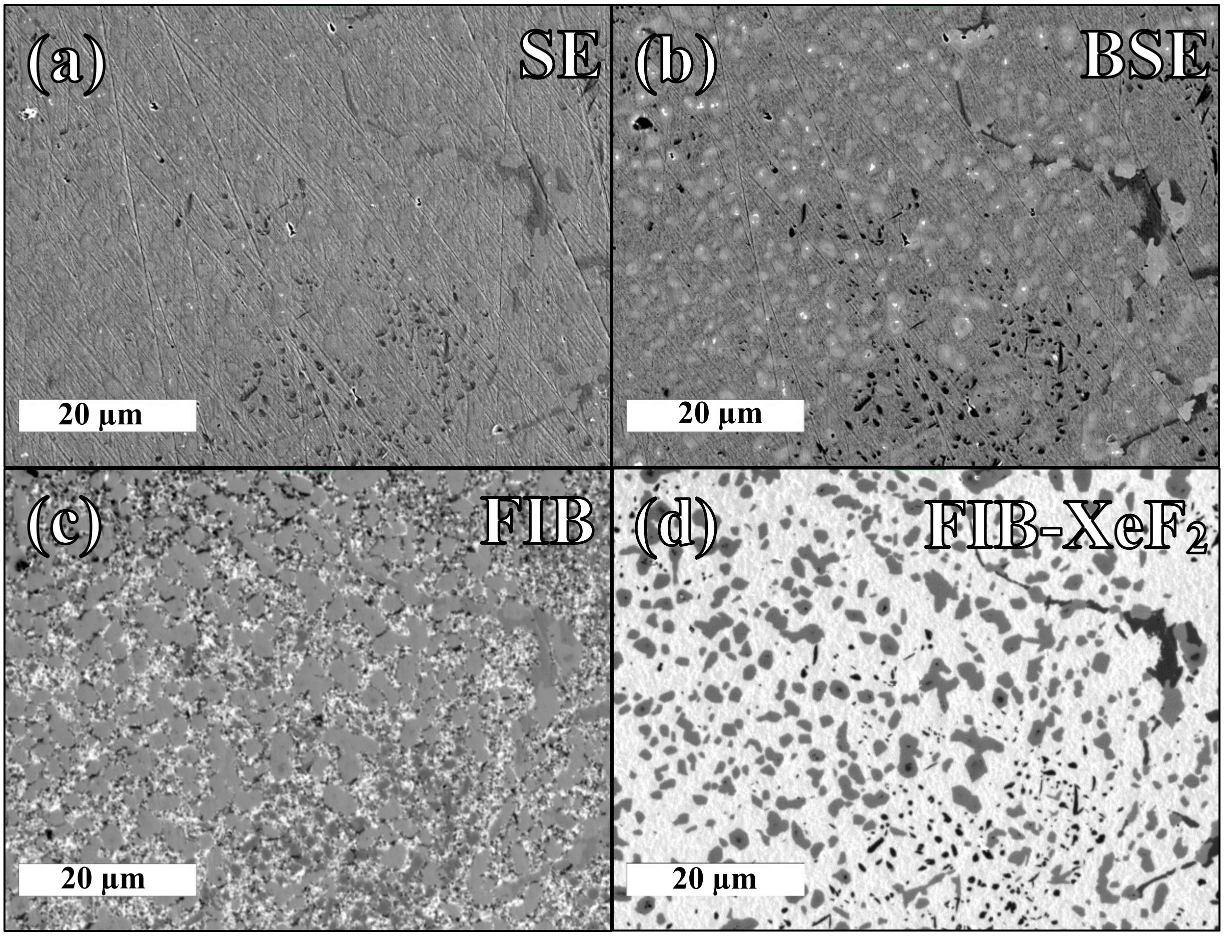

Figure 2: Microscopy images of the sample were taken in an area of interest. a) Secondary electron (SE) image, b) Backscattered Electron (BSE) image, c) Focused Ion Beam (FIB) image after a 20 s exposure to a high probe current. d) A focused ion beam XeF_2 (FIB-XeF_2) image of a steel sample after applying the XeF_2 mapping procedure outlined in this study. Different precipitates and their substructures can be observed in varying levels of greyscale depending on their work function.

Table 1: Description of the main regions of interest observed in Focused Ion Beam (FIB) micrographs and Transmission Kikuchi Diffraction (TKD) patterns for a carburised experimental Fe9Cr1Mo steel sample after the FIB-XeF_2 contrast mapping procedure outlined in this study.

Index	TKD ID	Greyscale brightness order	Shape	Aspect Ratio	Other
1	$M_{23}C_6$	1 - Lightest	Rounded/Blocky	Roughly equiaxed	Contains inner substructure
2	M_7C_3	2	Rounded/blocky	Elongated	Often connecting to object 1
3	No ID	3	Rounded	Equiaxed	Inner substructure (core) of object 1
4	M_2C	3 - Darkest	Rounded	Elongated	Clustered

Area Analysis

Slice analysis of each image by pixel row revealed the mean precipitate area fraction as a function of distance down the fin, see Figure 3. The mean precipitate area fraction for the region of interest (ROI) identified as $M_{23}C_6$ was significantly higher throughout than both M_7C_3 and M_2C and comprised much of the precipitate surface area found within the sample. M_7C_3 was the second most prevalent precipitate by surface area but not significantly more than M_2C.

The distribution of the summed precipitates showed a lower area fraction in the centre of the sample, where higher area fractions at the fin and bore sides were observed. The bore side exhibited the highest area fraction. The mean area fraction for $M_{23}C_6$ shows a similar distribution to what was revealed for the total precipitate distribution however, it was lower in the centre of the sample. Both M_7C_3 and M_2C had an increase in mean area fraction in the centre. For M_2C this was the main peak in its distribution, though for M_7C_3 there were also increases in mean area fraction at each end of the sample.

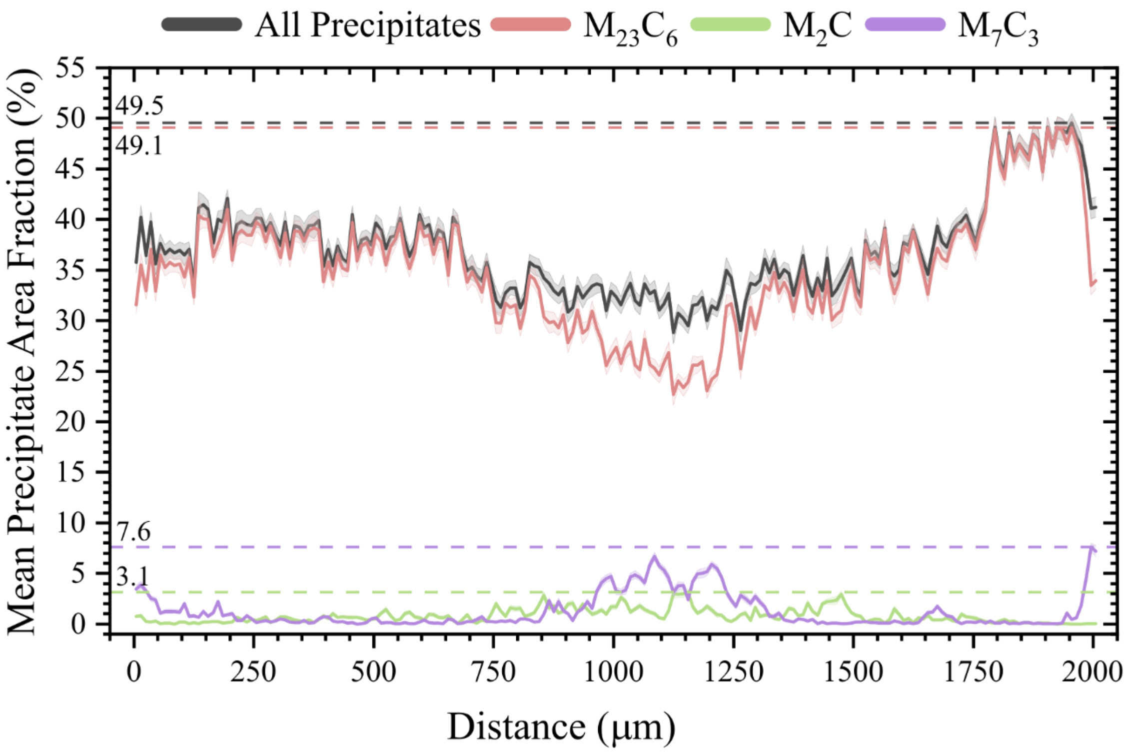

Figure 3: Mean area fraction for each region of interest (ROI) distinguished by the auto-Otsu thresholding process used in this study as a function of distance across a carburised Fe9Cr1Mo steel sample. Maximum mean precipitate area fraction values are labelled within the graph for each precipitate and for the total. Error bands were added with a moving standard deviation.

Object Analysis

Statistical analysis on objects within the multi-ROIs of $M_{23}C_6$, M_7C_3 and M_2C revealed: precipitate linear distribution by count (Figure 4.a), precipitate aspect ratio for the sample (Figure 4.b) and precipitate surface area for the sample (Figure 4.c).

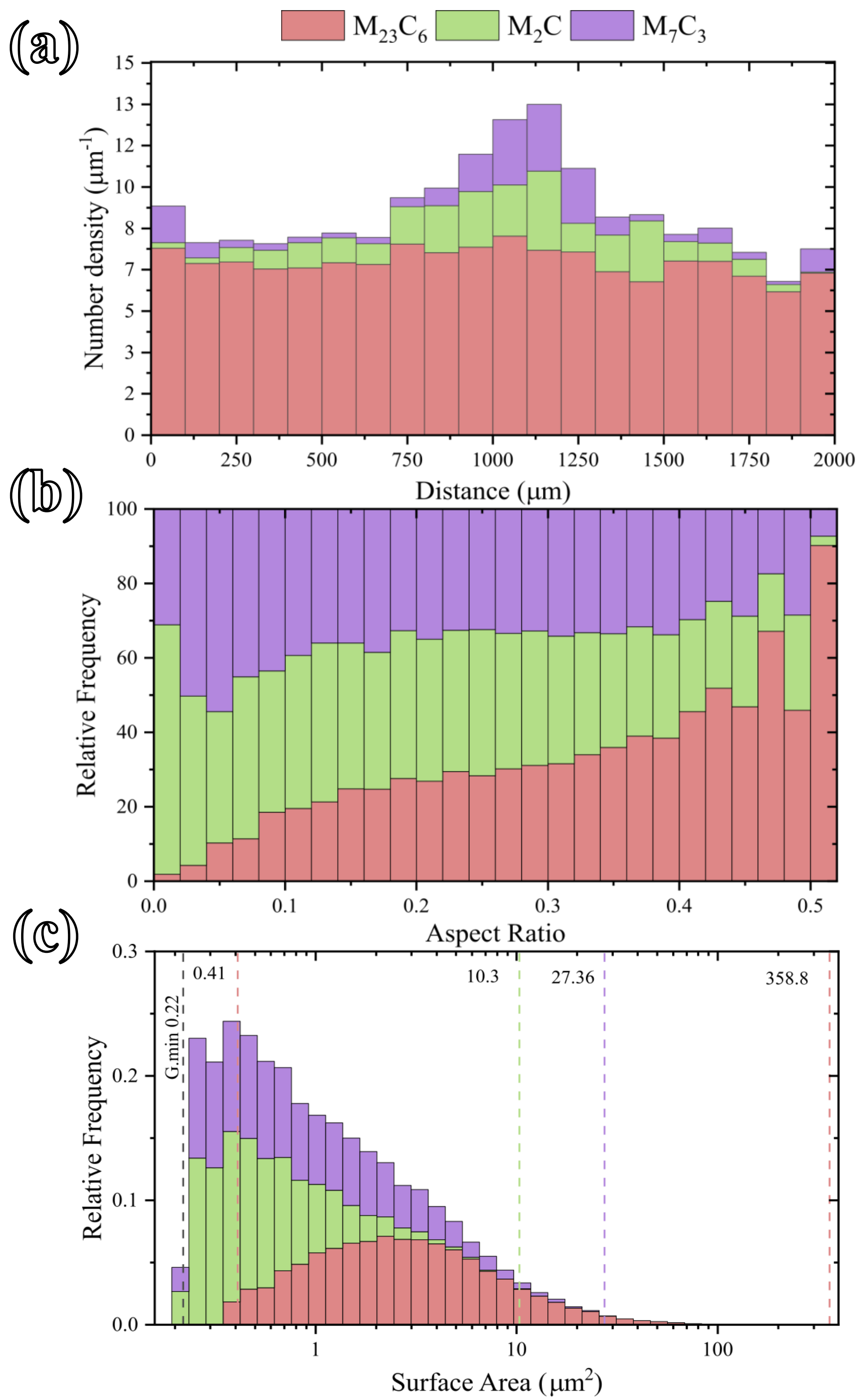

Figure 4: Statistical object analysis by precipitate type across a carburised Fe9Cr1Mo steel sample. a) Precipitate line number density. b) Aspect ratio distribution. c) Surface area distribution; reference lines: maximum values by type, with G.min referring to the minimum possible value due to data exclusion parameters.

The distributional data shown in Figure 4.a showed that $M_{23}C_6$ had a relatively uniform distribution across the Fe9Cr1Mo steel sample, with slight peaks at the start and middle of the sample. For M_7C_3, it showed a trimodal distribution, where peaks were present at the beginning middle and end of the sample. M_2C had a normal distribution centred on the middle of the sample. The aspect ratio data shown in Figure 4.b showed that $M_{23}C_6$ had a much higher relative fraction closer to 0.5 than both other precipitates. M_7C_3 slightly tends towards the lower end of the aspect ratio value and M_2C has a significantly higher fraction at the low end of the aspect ratio scale. The surface area data shown in Figure 4.c displays the global minimum precipitate surface area as 0.22 μm^2 due to the minimum voxel size of 50. Both M_7C_3 and M_2C had a minimum precipitate value equal to the global minimum, whereas $M_{23}C_6$ had a minimum precipitate size of 0.41 μm^2. $M_{23}C_6$ was the largest precipitate by a large margin, followed by M_7C_3 and then M_2C. $M_{23}C_6$ has a log-normal distribution, and M_7C_3 and M_2C had a positively skewed log-normal distribution.

DISCUSSION

In this study, we differentiate between different carbide precipitates and their substructure using FIB-XeF_2 contrast mapping on a steel sample which, after high temperature CO_2 exposure, has a complex population of different carbide precipitates. This technique not only allows us to clearly see precipitates and substructures within the steel but to also distinguish between those precipitates based on differences in ion-induced channelling contrast. By using this in conjunction with image processing it is relatively easy to obtain quantifiable statistical information over large area scales.

This technique provides high-resolution images and statistical analysis across very large sample areas. Providing clear visual distinction between precipitates and their substructures that is clearly superior to SE, BSE, or FIB imagery. By employing this technique with image processing within Dragonfly, we can gain quantitative statistical information on a pixel-by-pixel resolution across the sample at low magnification, and vastly improve the statistical resolution of the data achieved by image averaging (see Coghlan et al. (2020), (2021), Gong et al. (2023), Liu (2018), and Yan et al. (2018)). This is a semi-automated process, where the auto-Otsu threshold methodology removes a level of random user bias from identifying regions of interest. Data from large areas can be taken in a relatively short amount of time, especially when compared to techniques that give the same level of identification.

The methodology used in this study has many strengths but is not without its flaws. While the contrast map produced in Figure 2.d shows four distinct areas (see Table 1), the auto-Otsu threshold method was only able to differentiate three contrasts after separating the precipitates from the matrix. Unfortunately, this means that this leaves an object type unaccounted for and another type has been artificially inflated due to a similarity in greyscale with the unaccounted object type. Improvements in image processing would help solve the misidentification. This would likely take the form of the deep learning models within Dragonfly that would allow - in theory and after model training - the ROI identification based on: morphology, contrast and location (e.g. within other structures). Other minor limitations include the rejection of objects below a set size due to their similarity with small dust and dirt particles or pits.

In theory, this technique can be applied to a variety of other materials containing precipitates, with only minor adjustments to the methodology (current and exposure time). Those researching steels for use in harsh environments should take serious consideration in the use of this technique to identify precipitates. Firstly, to simply discover what is in your sample, FIB-XeF2 contrast mapping enables statistical mapping of precipitate types over large length-scales that would otherwise be missed using other techniques. Secondly, the precise datasets produced by the image recognition approach can identify quantifiable and statistical trends within a material based on precipitate size, location, shape, and orientation. The combination of these advanced characterisation and data analytical approaches provides new ways to understand the chemical and mechanical properties of complex materials on a micro and macro scale.

CONCLUSION

Precipitates within materials can cause many different problems for the material and its function. By using FIB-XeF_2 contrast mapping in conjunction and image processing, it was possible to characterise and extract statistical information on the major precipitate species in the material by type, distribution, size, and shape across large-scale areas in relatively small timeframes. Improvements on the technique include the use of deep learning models to better differentiate substructures exposed by ion-induced channelling contrast.

REFERENCES

Aassime, A and Hamouda, F. (2017). *Conventional and Un-Conventional Lithography for Fabricating Thin Film Functional Devices*, (Nikolay N. Nikitenkov, ed.), Rijeka, IntechOpen.

Advani, A. H., Murr, L. E., Atteridge, D. G., Chelakara, R., and Bruemmer, S. M. (1991). "Deformation Effects on Intragranular Carbide Precipitation and Transgranular Chromium Depletion in Type 316 Stainless Steels" *Corrosion*, 47 939–947.

Callister, W. D., and Rethwisch, D. G. (2020). *Materials science and engineering : an introduction*, Hoboken, NJ, Wiley Hoboken, NJ.

Coghlan, L. (2020). "Carburisation and its Effect on the Oxidation Characteristics of 9Cr-1Mo Steel".

Coghlan, L., Yan, S., Shin, A., Pearson, J., Jepson, M. A. E., and Higginson, R. L. (2020). "Dispersion of complex carbides at the oxidation front during the oxidation of 9Cr-1Mo steel" *Corrosion Science*, Pergamon, 165 108389.

Coghlan, L., Yan, S., Shin, A., Pearson, J., Jepson, M. A. E., and Higginson, R. L. (2021). "The effect of microstructure on the oxidation and carburisation of 9Cr-1Mo steel exposed to CO2" *Corrosion Science*, Pergamon, 191 109720.

Dragonfly [Computer Software]. (2022). Comet Technologies Canada Inc. software available at https://www.theobjects.com/dragonfly.

Ganczarczyk, A., Geller, M., and Lorke, A. (2010). "XeF2 gas-assisted focused-electron-beam-induced etching of GaAs with 30 nm resolution" *Nanotechnology*, 22 045301.

Gong, Y., Gill, S. P. A., Yan, S., Higginson, R., Sumner, J., Simms, N. J., Larsson, H., Shin, A., Pearson, J. M., Young, D. J., Atkinson, C., Cocks, A. C. F., and Reed, R. C. (2023a). "Assessment of corrosive attack of Fe9Cr1Mo alloys in pressurised CO2 for prediction of breakaway oxidation" *Corrosion Science*, 111385.

Gong, Y., Gill, S. P. A., Yan, S., Higginson, R., Sumner, J., Simms, N. J., Larsson, H., Shin, A., Pearson, J. M., Young, D. J., Atkinson, C., Cocks, A. C. F., and Reed, R. C. (2023b). "Assessment of corrosive attack of Fe9Cr1Mo alloys in pressurised CO2 for prediction of breakaway oxidation" *Corrosion Science*, 222 111385.

Hwang, S. S., Lim, Y. S., Kim, S. W., Kim, S. J., and Kim, H. P. (2013). "Role of grain boundary carbides in cracking behavior of Ni base alloys" *Nuclear Engineering and Technology*, 45 73–80.

Karunaratne, M. S. A., Yan, S., Thomson, R. C., Coghlan, L., and Higginson, R. L. (2020). "Modelling carburisation in 9Cr-1Mo ferritic steel tube substrates in experimental CO2 atmospheres" *Corrosion Science*, Pergamon, 163 108248.

Kettle, J., Hoyle, R. T., and Dimov, S. (2009). "Fabrication of Step-and-Flash Imprint Lithography (S-FIL) templates using XeF2 enhanced focused ion-beam etching" *Applied Physics A*, 96 819–825.

Lawson, R. A., and Robinson, A. P. G. (2016). "Chapter 1 - Overview of materials and processes for lithography" in A. Robinson and R. Lawson (Eds.), *Frontiers of Nanoscience*, Elsevier, 1–90.

Li, J., Zhang, P., He, T., Cheng, L., Wang, L., and Li, H. (2019). "Effect of carbides on high-temperature aging embrittlement in 12%Cr martensitic heat-resistant steel" *Journal of Materials Research and Technology*, 8 5833–5846.

Liu, C. (2018). "Oxidation and carburisation of 9Cr-1Mo steel in both simulant and in-service AGR coolant gases".

Liu, C., Heard, P. J., Payton, O. D., Picco, L., and Flewitt, P. E. J. (2019). "A comparison of two high spatial resolution imaging techniques for determining carbide precipitate type and size in ferritic 9Cr-1Mo steel" *Ultramicroscopy*, 205 13–19.

Liu, J., Li, L., Yang, S., Ding, C., Wang, E., Yu, X., Wu, H., and Niu, G. (2023). "Effect of intragranular κ carbides and intergranular precipitates on the hot deformation mechanism and dynamic recrystallization mechanism of Fe–28Mn–11Al–1.5C–5Cr lightweight steel" *Journal of Materials Research and Technology*, 27 2346–2362.

N. Otsu. (1979). "A Threshold Selection Method from Gray-Level Histograms" *IEEE Transactions on Systems, Man, and Cybernetics*, 9 62–66.

Petzow, G., Koch, R., and Nelson, J. A. (1978). *Metallographic etching : metallographic and ceramographic methods for revealing microstructure*, Metals Park, Ohio, American Society for Metals Metals Park, Ohio.

Ray, V., Oboňa, J. V., Sharang, S., Rotkina, L., Chang, E., and Tolua, K. (2016). "Optimizing Gas-Assisted Processes for Ga and Xe FIB Circuit Edit Application" 397–401.

Yan, S., Doak, S., Thomson, R., and Higginson, R. (2018). "An investigation on oxidation/carburisation of 9Cr-1Mo steel heat exchanger tube in an AGR environment" *Materials at High Temperatures*, Taylor and Francis Ltd., 35 56–65.

Young, D. J., and Zhang, J. (2018). "Alloy Corrosion by Hot CO 2 Gases" *JOM*, 70.